Dual-Enzyme-Loaded Multifunctional Hybrid Nanogel System for Pathological Responsive Ultrasound Imaging and T_2-Weighted Magnetic Resonance Imaging

Xia Wang,[†] Dechao Niu,[‡] Pei Li,[§] Qing Wu,[†] Xiaowan Bo,[§] Boji Liu,[§] Song Bao,[†] Teng Su,[†] Huixiong Xu,[*,§] and Qigang Wang[*,†]

[†]Department of Chemistry and Advanced Research Institute, Tongji University, Shanghai, 200092, China, [‡]Lab of Low-Dimensional Materials Chemistry, Key Laboratory for Ultrafine Materials of Ministry of Education, School of Materials Science and Engineering, East China University of Science and Technology, Shanghai, 200237, China, and [§]Department of Medical Ultrasound, Shanghai Tenth People's Hospital, Tenth People's Hospital of Tongji University, Shanghai, 200072, China,

ABSTRACT A dual-enzyme-loaded multifunctional hybrid nanogel probe (SPIO@GCS/acryl/biotin-CAT/SOD-gel, or SGC) has been developed for dual-modality pathological responsive ultrasound (US) imaging and enhanced T_2-weighted magnetic resonance (MR) imaging. This probe is composed of functionalized superparamagnetic iron oxide particles, a dual enzyme species (catalase and superoxide dismutase), and a polysaccharide cationic polymer glycol chitosan gel. The dual-modality US/MR imaging capabilities of the hybrid nanogel for responsive US imaging and enhanced T_2-weighted MR imaging have been evaluated both *in vitro* and *in vivo*. These results show that the hybrid nanogel SGC can exhibit efficient dual-enzyme biocatalysis with pathological species for responsive US imaging. SGC also demonstrates increased accumulation in acidic environments for enhanced T_2-weighted MR imaging. Further research on these nanogel systems may lead to the development of more efficient US/MR contrast agents.

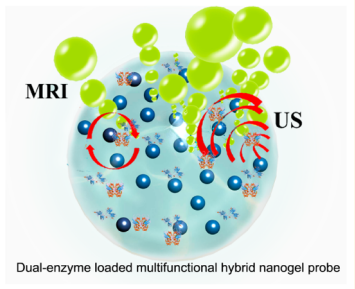

Dual-enzyme loaded multifunctional hybrid nanogel probe

KEYWORDS: hybrid nanogels · pathological responsiveness · ultrasound imaging · magnetic resonance imaging

Over the past few decades, unprecedented progress has been made in the diagnosis and detection of many diseases, especially various forms of cancer. Various imaging techniques including ultrasound (US) imaging, magnetic resonance (MR) imaging, computed tomography (CT), positron emission tomography (PET), and optical microscopy have been widely employed to gain diagnostic information and determine efficient and safe therapies.[1] Among all of these imaging techniques, US imaging is the most commonly used despite its relatively low resolution, due to its low cost, facile operation, real-time capabilities (more than 200 fps), and ability to image structure and function simultaneously. In contrast, MR imaging has excellent spatial resolution and is believed to be one of the most powerful diagnostic tools currently available. However, MR imaging often has problems with low sensitivity.[2] However, the combination of US and MR imaging can offer complementary medical information for the diagnosis of various diseases.

In general, dual-mode contrast agents are necessary in order to further enhance the accuracy and efficacy of imaging techniques. Once the contrast agents enter the specific tissues of interest, they can reveal exact sizes and characteristics of the abnormalities present.[3,4] Microbubble-based agents loaded with superparamagnetic iron oxide (SPIO) nanoparticles[5−7] and microbubbles functionalized with gadolinium complexes[8] have been constructed and shown to enhance both US and MR imaging simultaneously. Recently, Shi and co-workers developed manganese-functionalized inorganic nanosized silica systems encapsulated by perfluorocarbon and loaded with

* Address correspondence to wangqg66@tongji.edu.cn, xuhuixiong@hotmail.com.

Received for review November 30, 2014 and accepted June 2, 2015.

Published online June 02, 2015
10.1021/nn5068094

SPIO particles.[9,10] Enhanced US and MR imaging was achieved due to the nanosize and high stability of these inorganic agents. The presence of SPIO nanoparticles and monodispersed manganese in this system as well as the large number of phase-changed perfluorocarbon microbubbles present under intensified US irradiation contributed to the effective enhancement of the MR and US imaging. However, there is still room for improvement, in particular achieving more effective accumulation of the agent within the target tissue with smaller side effects. To address this, one strategy is to provide the contrast agent with the ability to respond to stimuli in the biological microenvironment of the target area.[11] The abnormalities found in the biological microenvironment relative to normal tissue, such as those concerning vascular activity, oxygenation, perfusion, pH, and overexpressed enzymes, are the basis for any corresponding diagnostic and therapeutic strategies.[12−14] Rao and co-workers have also designed specific nanosensors for the rapid, real-time *in vivo* imaging of reactive oxygen or nitrogen species as well as caspase-3/7, allowing for the direct evaluation of acute hepatotoxicity and tumor apoptosis.[15,16]

Specifically, reactive oxygen species (ROS) are often induced by inflammation,[17] which is the first response of the immune system to protect against infection, irritation, or injury and is associated with many diseases including cancer, atherosclerosis, asthma, and cystic fibrosis.[18] Detection of ROS, including hydrogen peroxide (H_2O_2), superoxide anions ($O_2^{\bullet-}$), and hydroxyl radicals ($^{\bullet}OH$), can provide important physiological and biological information about the state of the living system. Recent progress in the fields of biomedicine and nanotechnology has enabled the development of various nanoprobes that detect abnormally high levels of ROS for responsive biomedical imaging of pathological tissues. Fluorescent and luminescent probes are also usually designed for the detection of ROS.[19] Due to the intracellular acidification of pathological tissues, there have been a wide variety of studies conducted on lower-pH responsive tumor imaging. The large amount of pH-responsive fluorescent molecular and acid-labile polymers developed for this type of imaging make it a relatively easy-access and effective technique.[20,21] Less research has focused on the detection of pathological tissues using US and MR imaging. Gu and co-workers were the first to observe the catalytic breakdown of H_2O_2 into oxygen by Prussian blue nanoparticles (KFe^{3+} $[Fe^{2+}(CN)_6]$). The paramagnetic oxygen bubbles formed by this technique can be used to simultaneously enhance both US and T_1-weighted MR imaging.[22]

On the basis of this pioneering work, we designed a dual-enzyme-loaded multifunctional hybrid nanogel system for dual-modality noninvasive pathological responsive US and T_2-weighted MR imaging. The probe is composed of ROS-responsive enzymes and a polysaccharide cationic polymer glycol chitosan nanogel functionalized with SPIO nanoparticles. This probe can therefore react with ROS within the biological system and generate bubbles for enhanced US imaging, while also accumulating in high amounts in acidic environments for enhanced T_2-weighted MR imaging. As an emerging material, the nanogel system is a hydrogel nanoparticle possessing three-dimensional hydrophilic networks,[23,24] similar to macro-hydrogels.[25−27] Its ideal fluid-like transport properties and hydrophilic environment make the nanogel a perfect candidate for biocatalysis, biomedical diagnosis, and therapy.[28−31] The immobilization (encapsulation) of enzymes within the gel matrix provides protection from structural alterations and subsequent deactivation of the enzymes, ensuring higher loadings and better substrate mobility for efficient catalysis.[32−34] In addition, the unique hydrophilic environment and water-rich structure of this nanogel make it an ideal probe for MR imaging,[35−37] where the signal detected is directly related to relaxation time.[38] In this work, focused on exploiting the structure−function relationships of the hydrogel, the dual-enzyme-loaded multifunctional magnetic nanogel can be developed to be an efficient and safe probe for dual-modality pathological responsive US and T_2-weighted MR imaging.

RESULTS AND DISCUSSION

The proposed design of the multifunctional hybrid nanogel, designated as SGC (SPIO@GCS/acryl/biotin-CAT/SOD-gel), is shown in Scheme 1. Our design includes the functionalization of the glycol chitosan monomer (GCS) followed by hydrophilic/hydrophobic interactions and electrostatic attraction between the monomer and the SPIO particles and dual enzymes (catalase and superoxide dismutase) in the buffers. The fabrication process is completed by subsequent mild enzymatic polymerization and generation of the corresponding nitroxide radicals from laccase-catalyzed hydrogen abstraction by NHS,[39] which has been previously reported as an efficient and mild gelation procedure by our group.[40−42] The selected catalase (CAT) and superoxide dismutase (SOD) play an important role in maintaining the redox balance of the living organisms by scavenging excess ROS.[43,44] The dual-enzyme-loaded hybrid nanogel efficiently enables the catalytic reaction with both the $O_2^{\bullet-}$ and H_2O_2 species in the pathological environment to generate molecular oxygen. The oxygen then forms bubbles, which can change the acoustic impedance of the tissue and enhance the US imaging. Concurrently, the nanogel layer around the SPIO particles also simultaneously lowers the molecular diffusion coefficient of water[35,45,46] and increases the transverse relaxation rate, resulting in an enhancement of T_2-weighted MR imaging according to the Bloembergen−Purcell−Pound theory.[47] When

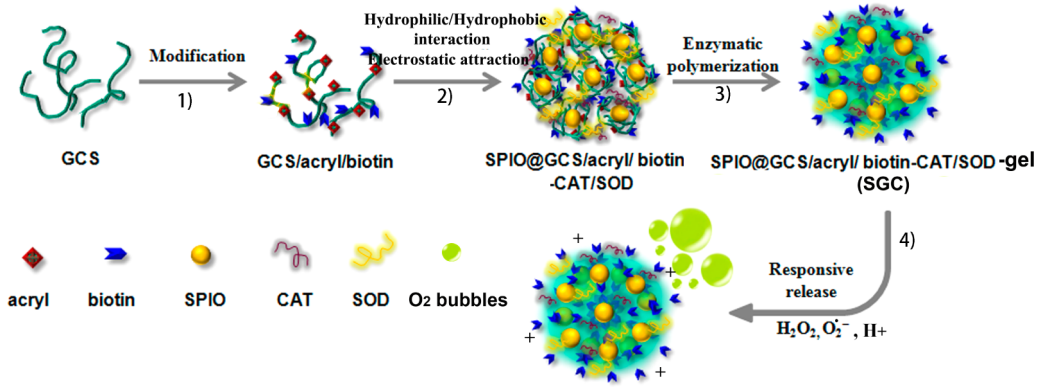

Scheme 1. Schematic illustration of the SGC (SPIO@GCS/acryl/biotin-CAT/SOD-gel) nanogel. The fabrication process of SGC involves (1) modification of acryl bonds and the biotin group on glycol chitosan (GCS), (2) interaction between the modified glycol chitosan and the superparamagnetic iron oxide particles (SPIO), as well as electrostatic attraction of the dual enzymes (CAT: catalase, SOD: superoxide dismutase), (3) efficient enzymatic polymerization of the above hybrid system, and (4) responsive bubble generation and protonation effect due to pathological stimuli (H_2O_2, $O_2^{\bullet-}$, and H^+) for enhanced dual-modality US/MR imaging.

entering an acidic pathological microenvironment, the pH-sensitive glycol chitosans adopt a more cationic surface. This results in improved accumulation of SGC in the target area and facilitates enhancement of both US and T_2-weighted MR imaging.[48] In other words, after interacting with pathological stimuli (H_2O_2, $O_2^{\bullet-}$, and H^+) *in vivo*, the specific hybrid nanogel SGC potentially serves as a highly efficient dual-modality US/MR contrast agent for pathological detection, including but not limited to malignancy.

Construction and Characterization of SGC. The morphology, structure, and *in vitro* performance of SGC were characterized first as shown in Figure 1. The uniform spherical morphology of SGC with highlighted SPIO particles (approximately 13 nm shown in Figure S1 in the Supporting Information, SI) is observed in the scanning transmission electron microscopy (STEM) images using different modes (SE, HAADF, and BF, respectively). This morphology is also observed in energy-dispersive X-ray spectroscopy (EDS) mapping (Figure 1a) and transmission electron microscopy (TEM) images (see Figure S2 in the SI). The X-ray diffraction (XRD) patterns of SGC shown in Figure 1b exhibited the expected strong diffraction peaks from Fe_3O_4. In addition, the quantity of Fe was calculated as approximately 24 wt % of SGC using inductively coupled plasma atomic emission spectroscopy (ICP-AES). SGC also possesses an average dynamic diameter of 218 nm (Figure 1c) and is well dispersed in the phosphate buffer solution (PBS) with an obvious Tyndall effect, indicating favorable hydrophilicity of the SGC nanogels (Figure S3 in the SI). Zeta potentials at different pH values (Figure 1d) indicate that the surface charge of SGC increases from nearly 0 to about +18.7 mV as the pH decreases from 7.4 to 6.5. This sensitivity to pH gives SGC excellent stability during circulation and may also contribute to enhanced accumulations in acidic pathological microenvironments at pH <7.4.[48] Before loading the bioactive enzymes (CAT and SOD), the successful removal of tetrahydrofuran (THF) from the system was confirmed by the NMR spectra of the SPIO@GCS/acryl/biotin cluster before and after the dialysis process (Figure S4 in the SI).

The FT-IR spectrum (Figure S5) of SGC was also measured to verify the presence of various functional components. The strong peak at 540 cm^{-1} is attributed to the iron oxide skeleton (Fe−O), while the bands near 1643, 1534, and 1404 cm^{-1} are characteristic of the carboxylate groups (COO−) of iron-oleate.[49,50] The spectra of both glycol chitosan and SGC reveal absorption bands characteristic of chitosan (N−H at 1656 cm^{-1}) and a PEG group (−C−O−C− at 1057 cm^{-1}, $-CH_2-$ at 2932 cm^{-1}, −CH− at 2864 cm^{-1}, and a hydroxyl group around 3400 cm^{-1}).[51,52] The increased intensity of the peaks at 1656 and 1534 cm^{-1} in the SGC spectrum belong to the $-NH_2$ group in chitosan and the protein amide band from CAT and SOD.[53] On the basis of these results, the composition of SGC nanogels was verified to be the enzyme-loaded SPIO-functionalized polysaccharide glycol chitosan nanosystem.

In addition, the loading amount and activity of the dual enzymes (CAT and SOD) in the nanogel system were evaluated by UV−vis spectroscopy, as shown in Table S1 and Figure S6. The CAT and SOD loading amount were calculated to be approximately 60 and 13 wt % of SGC, respectively (Figure S6a and b). The enzyme activities were evaluated based on the ability of CAT to catalyze H_2O_2 degradation and SOD to inhibit the autoxidation of pyrogallol (Figure S6c and d). The CAT and SOD enzymes within SGC retain 82% and 69% of their activity, respectively, relative to the free enzymes. After being stored at 4 °C for 30 days, CAT and SOD retained 66% and 60% of their enzymatic activity, respectively (Figure S7). The relatively high activities of CAT and SOD within the SGC nanogel make it a potential responsive contrast agent for US imaging.

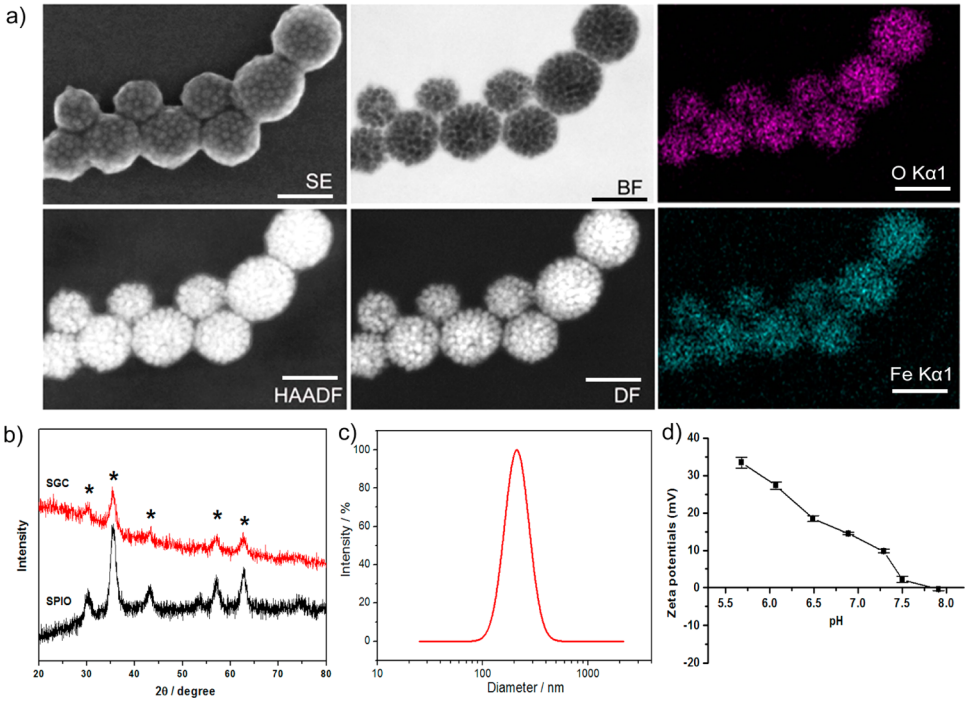

Figure 1. Characterization of SGC. (a) Scanning transmission electron microscopy (STEM) images of SGM using different modes and energy dispersive X-ray (EDX) spectroscopy mapping images of the O and Fe elements (SE: second electronic, HAADF: high-angle annular dark field, BF: bright field, DF: dark field). The scale bars in (a) indicate 50 nm. (b) XRD patterns of the SPIO particles and SGC (* indicate the diffraction peaks of Fe_3O_4). (c) Diameter distributions in PBS by dynamic light scattering (DLS) measurements. (d) Zeta potentials of SGC (n = 3) at different pH values.

***In Vitro* Responsive US and T_2-Weighted MR Imaging Capability of SGC.** As a potential dual-modality contrast agent for US and MR imaging, the *in vitro* responsive bubble generation and magnetic properties of SGC were evaluated, as shown in Figure 2. The *in vitro* bubble generation from SGC was investigated in a simulated pathological environment (50 μM H_2O_2 solution) and observed *via* an optical microscope (Figure 2a,b). As expected, a large number of microbubbles emerged after the H_2O_2 solution was injected into the SGC solution, namely, as SGC/H_2O_2 (5 mg/mL SGC in 50 μM H_2O_2 solution). The control solution (50 μM H_2O_2 solution) did not generate any obvious microbubbles in the area investigated (Figure S8 in the SI). These results indicate that H_2O_2 can be efficiently and rapidly converted into molecular oxygen in about 10 s. In addition, oxygen generation is faster than diffusion, resulting in the accumulation of oxygen bubbles, which is ideal for contrast in US imaging. Within a relatively isolated system, the oxygen microbubbles remain stable up to 12 h without any further merging and diffusing, which is also favorable for efficient US imaging.[54]

On the other hand, the magnetic properties and *in vitro* T_2-weighted MR imaging capabilities of SGC were also studied. The SPIO nanoparticles within this system have a saturation magnetization (M_s) value of 60.3 emu·g^{-1} and an r_2 relaxation value of 154.8 $mM_{Fe}^{-1}\cdot S^{-1}$, indicating excellent magnetization properties for use in MR imaging (Figures S9 and S10 in the SI). As shown in Figure 2d, no hysteresis loop is observed from the magnetization curve collected at room temperature, which demonstrates the superparamagnetic nature of SGC. The M_s value of the dried SGC is 29.1 emu·g^{-1}, which is significantly higher than the magnetic clusters encapsulated in a polymer matrix or mesoporous structure.[55,56] To evaluate the MR imaging capabilities of SGC, the transverse relaxivity was also measured using a clinical 3.0 T MRI scanner. In Figure 2e, the SGC solutions are observed to become darker in T_2-weighted MR images as Fe concentration is increased, indicating excellent MR imaging capability. Additionally, the r_2 value of SGC (478 $mM_{Fe}^{-1}\cdot S^{-1}$) is significantly higher than most iron oxide-based MR contrast agents[57] (see Table S2 in the SI for further details). The high r_2 value of SGC may be attributed to the high Fe loading amount (24 wt %) of SGC, resulting in a high M_s value and enhanced *in vitro* MR imaging.[58] Another reason for the high r_2 value may be the unique nanogel network surrounding the SPIO nanoparticles, which can lower the water diffusion coefficient and therefore increase the transverse relaxation rates. Together, these results demonstrate the *in vitro* efficiency of the hybrid nanogel SGC as a dual-modality US/MR contrast agent for the detection of pathological ROS and acid-sensitive US and T_2-weighted MR imaging (Figure 2c).

***In Vivo* US Contrast Imaging.** Before conducting *in vivo* experiments, the cytotoxicity and cytophagy of the SGC nanogels were evaluated on human liver hepatocellular HepG2 cells. The viability of the HepG2 cells

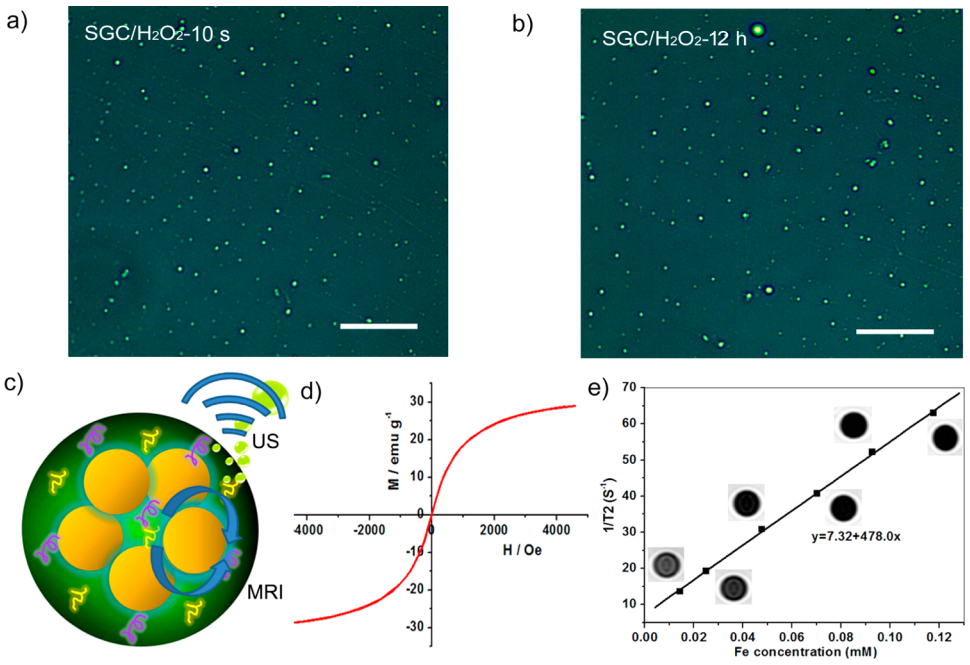

Figure 2. *In vitro* **responsive bubble generation and magnetic properties of SGC: The** *in vitro* **bubble generation from SGC in the simulated pathological environment (50 μM H_2O_2 solution) at various times (a, b) and the scheme of SGC for enhanced US and MR imaging in this nanogel system (c). (d) Field-dependent magnetization curves (*M*−*H*) of the SGC nanoparticles at 300 K using a vibrating-sample magnetometer (VSM) and (e)** *in vitro* **MR T_2 signals** *versus* **Fe concentration at pH = 7.4. Transverse relaxivities (r_2) were derived from linear fitting of the plots. The scale bars in (a) and (b) indicate 50 μm.**

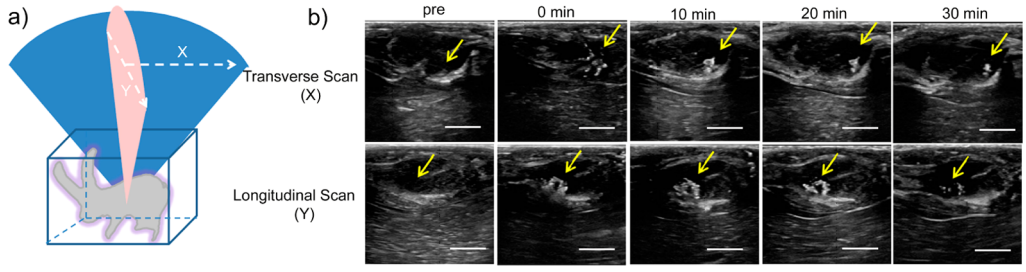

Figure 3. (a) Scheme and (b) US imaging of rabbits bearing VX2 tumors before and after intratumoral injection of SGC at different times using both transverse scanning and longitudinal scanning modes. Yellow arrows indicate injection positions in the VX2 tumors. The bars in (b) indicate 0.5 cm.

after incubation for 12 and 24 h with SGC ranging in concentration from 100 to 1000 μg/mL was above 90% in all cases (Figure S11 in the SI). These results indicate that the glycol chitosan-based nanogels possess good biocompatibility. In the cytophagy tests, the fluorescein isothiocyanate (FITC) was conjugated to SGC (FITC-SGC) to facilitate observation by confocal laser scanning microscopy (CLSM) (Figures S12 and S13 in the SI). Green fluorescence from FITC can be detected in the CLSM images of the HepG2 cells after co-incubation with FITC-SGC at different concentrations (25, 50, and 100 μg/mL) for different amounts of time (4 and 8 h). These images reveal successful uptake of the hybrid nanogels by the cells. With increased concentrations and prolonged incubation, more SGC with green fluorescence could be incorporated into HepG2 cells by endocytosis. These results indicate that SGC can be taken up by HepG2 cells and demonstrates relatively low cytotoxicity, which makes it suitable as a contrast agent for *in vivo* US and MR imaging.

In order to confirm the responsively enhanced imaging of pathologies, US imaging of rabbits bearing VX2 tumors after intratumoral injection of SGC (1 mL at 5 mg/mL) was conducted (Figure 3). Both the transverse (*x* axis) and longitudinal scan (*y* axis) signals at different time intervals (0, 10, 20, and 30 min) were recorded in order to demonstrate increased US acoustic gray values in images after intratumoral injection of SGC (Figure 3a). As shown in Figure 3b, the gray scale of the VX2 tumor is relatively low before injection. However, immediately after injection of SGC, the tumor tissue brightens immediately due to the fast reaction between the dual enzymes (CAT and SOD) in the SGC nanogel and the ROS ($O_2^{\bullet-}$ and H_2O_2 species). These results are in agreement with *in vitro* results showing high efficiency of this enzyme-loaded hybrid nanogel

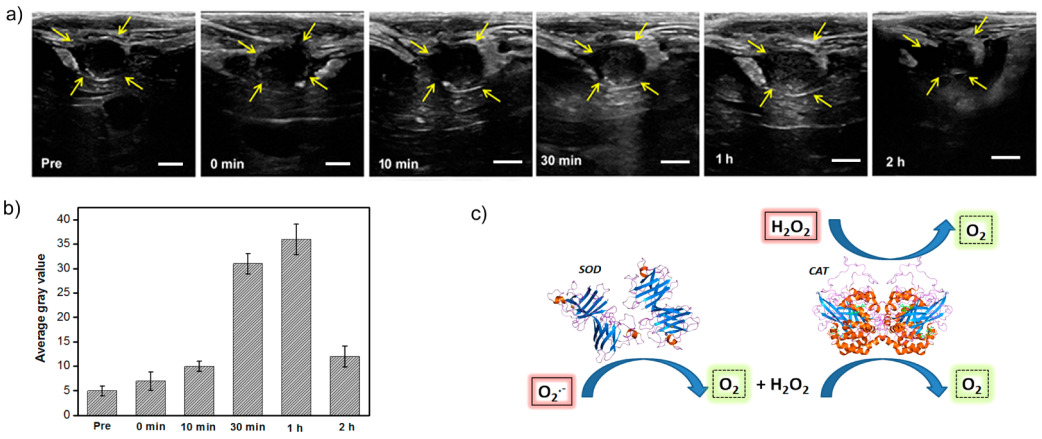

Figure 4. *In vivo* **US imaging. (a) US imaging and (b) the corresponding average gray values of VX2 tumors on rabbit livers before and after intravenous injection of SGC at various times. (c) Schematic mechanism of responsive bubble generation for US imaging. (d) The yellow arrows indicate outlines of the VX2 tumors. The bars in (a) correspond to 0.5 cm. The standard deviation in (b) is derived from a group within the region of interest (ROI) (*n* = 3).**

system (Figure 2a). A video of US imaging during the rejection process can be found in the SI. More remarkably, enhanced US imaging of the tumor tissue is still apparent 20 min after injection, which can be attributed to the diffusion of SGC into the interstitial tumor tissue as well as continuously emerging bubbles in response to the US wave. Approximately 30 min after injection, the gray value decreases due to diffusion of the bubbles and reduced amounts of reactive ROS.

To further verify the efficiency and safety of SGC, first US images after the intratumoral injection of SGC and single-SOD-loaded nanogel (SPIO@GCS/acryl/biotin-SOD-gel, abbreviated as SGC-SOD) were conducted at a lower density of 1 mg/mL (Figure S14). After injection, the tumor tissue brightened immediately, and the image was also significantly enhanced 10 min after intratumoral injection of either dual-enzyme-loaded SGC or single-SOD-loaded SGC-SOD. Furthermore, acridine orange (AO)/ethidium bromide (EB) (Figure S17) and annexin V-FITC/propidium iodide (PI) double staining (Figure S18) of HepG2 cells after co-incubation with SGC at 5 mg/mL for different times (4 and 8 h), as well as the pathological experiments with related tumor tissues by hematoxylin/eosin staining (Figure S19) after intratumoral injection of SGC (1 mL at 5 mg/mL), were investigated. The cell death and apoptosis staining experiments indicate that most of the cells were alive, and SGC has no discernible impact on cell apoptosis at the maximum working concentration. In addition, no significant damage was found in the observed tissue samples. These results confirm that the enzyme-loaded hybrid nanogel SGC has excellent potential as a responsive contrast agent for stable and effective US imaging.

US contrast imaging was also evaluated at various time intervals on the rabbit model bearing VX2 liver tumors after intravenous injection of SGC *via* ear vein. *In vivo* US images (Figure 4a) and their corresponding gray scales (Figure 4b) at different time intervals (0 min, 10 min, 30 min, 1 h, and 2 h) after intravenous injection of SGC (2 mL at 5 mg/mL) were investigated. Prior to injection, the tumor exhibited a relatively low acoustic signal. The corresponding average gray scales prior to, during, and 10 min after injection were approximately 5.1, 6.9, and 10, respectively. However, 30 min after injection and blood circulation the tumor tissues became considerably more brightened, with a significantly increased average gray scale of 31. After an additional 30 min of circulation, even more enhanced tumor imaging was observed, which can be attributed to the efficient accumulation of SGC particles in the tumor and their diffusion into the tumor interstitial tissue *via* passive enhanced permeability and retention (EPR) effects. These effects lead to increased formation of bubbles from the enzyme-loaded SGC, effectively enhancing tumor signals with an average gray scale of 36, which is approximately a 7-fold increase relative to preinjection. The gray value of the tumor subsequently decreased to approximately 12, which is consistent with the intratumoral injection experiment. The proposed reaction mechanism is shown in Figure 4c. The mechanism begins with the conversion of superoxide ($O_2^{\bullet-}$) to hydrogen peroxide (H_2O_2) and molecular oxygen by SOD and the subsequent conversion of H_2O_2 to water and molecular oxygen by CAT. The rapid accumulation of oxygen (O_2) leads to the formation of bubbles, which provide excellent contrast during US imaging. This contrast may also be attributed to a favorable gel lattice that ensures fast and effective catalytic reactions that fully utilize ROS present in pathological tissue. The dual-enzyme-loaded hybrid nanogel SGC can therefore be used as a responsive contrast agent for efficient US imaging.

***In Vivo* T_2-Weighted MR Contrast Imaging.** As a dual-modality contrast agent, SGC-based T_2-weighted MR imaging was further investigated *in vivo* for the rabbit model bearing VX2 tumors on the livers (Figure 5). Both the T_2-weighted MR images and their corresponding

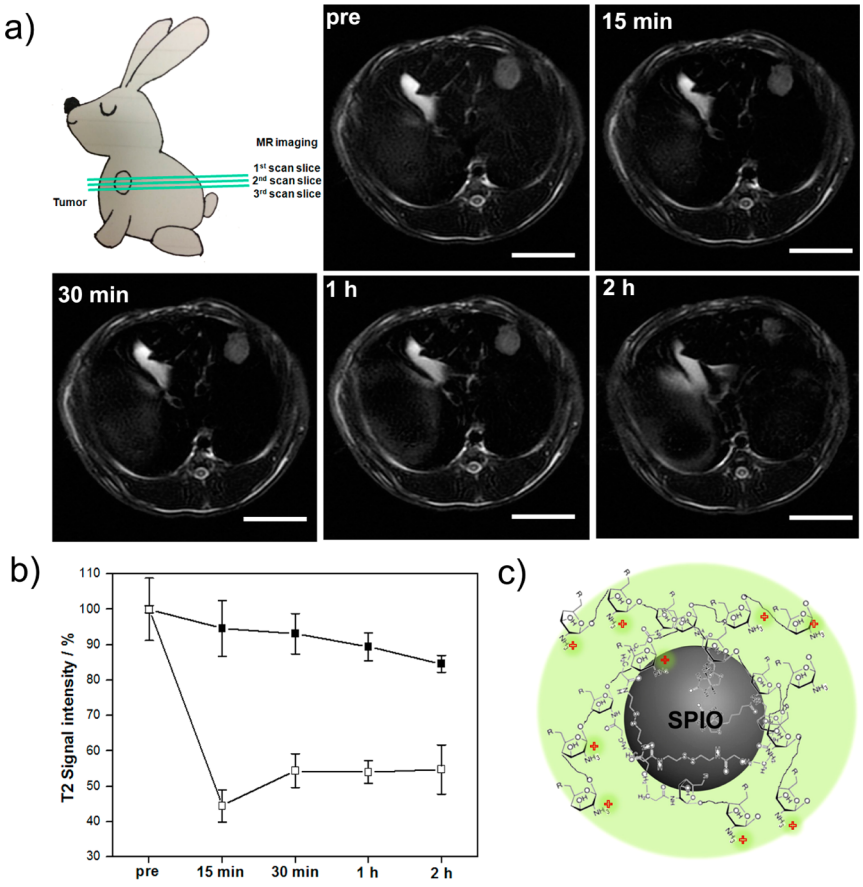

Figure 5. *In vivo* T_2**-weighted MR imaging. (a)** T_2**-weighted MR images and (b) their corresponding signal intensities for rabbits bearing VX2 tumors on the livers preinjection and 15 min, 30 min, 1 h, and 2 h after intravenous SGC injection. (c) Schematic mechanism of enhanced MR imaging. The standard deviation of the signal intensities is derived from a group within the ROI (*n* = 3). L and T in the image refer to the liver and tumor, respectively. The bars in (a) correspond to 2.0 cm.**

signal intensities at 15 min, 30 min, 1 h, and 2 h after SGC injection were recorded. The signal intensity of a single time point was averaged from three slices near the region of interest (ROI) (Figure 5a). The results showed that the T_2 signal of the normal liver tissues decreases sharply (approximately 56%) 15 min after the administration of SGC, as shown in Figure 5b, indicating significant retention of SGC in the liver. The decrease in the T_2 signal can be attributed to the phagocytosis of the reticuloendothelial system (RES) (*e.g.*, Kupffer cells in the liver).[59] Concentrations of SGC in the liver reach ~49.8 ng/mg (nanograms of Fe per milligram of tissue), as calculated by the time-dependent biodistribution of SGC using ICP-AES analysis (see Figure S18 in the SI). Further circulation results in an increase in signal intensity of approximately 46%. This result is consistent with ICP-AES results, which show less SGC accumulation 1 h (35.7 ng/mg) and 2 h (24.4 ng/mg) after injection.

In contrast, a significantly darker tumor signal is observed relative to the preinjection image. This darker tumor signal is detected 30 min, 1 h, and 2 h after injection, with declines in brightness of 7.0%, 11%, and 16%, respectively. The darker signal observed 1 and 2 h after injection corresponded to SGC concentrations in the tumor of 21.5 and 24.0 ng/mg, respectively. This result suggests that the SGC nanoparticles are accumulating and entering into the tumor region. Accumulation of SGC within the tumor was further confirmed by *ex vivo* Prussian blue staining of tumor tissue extracted from the rabbits immediately after *in vivo* MR imaging 2 h after injection of SGC (Figure S19). At this time, parts of the tumor tissues were also stained blue, indicating the accumulation of iron oxide-based SGC within the tumor areas.

A mechanistic scheme illustrating the ability of SGC to act as a highly efficient T_2 contrast agent in MR imaging is shown in Figure 5c. The magnetic particles within the nanogel matrix significantly enhance the transverse relaxation rate of the gel by lowering the diffusion coefficient of water in order to generate strong MR signals while also increasing SGC accumulation in the targeted acidic environment.[48] Therefore, the dual-enzyme-loaded multifunctional hybrid nanogel system SGC may be used as a new nanoprobe for efficient enzyme-responsive US imaging. In addition, the favorable hydrophilic hydrogel environment around the SPIO particles as well as the acid-sensitive

accumulation of SGC makes it an excellent contrast agent for enhanced T_2-weighted MR imaging.

CONCLUSIONS

In summary, a dual-enzyme-loaded multifunctional hybrid nanogel was designed and constructed for highly efficient pathological responsive US and T_2-weighted MR imaging. The favorable design of the SGC agent facilitates a fast and effective enzymatic reaction to generate a sufficient amount of oxygen (O_2) bubbles for contrast in US imaging. This SGC agent also exhibits increased accumulation in the acidic environment of the targeted areas and ensures encapsulation of the SPIO particles within the hydrogel in order to significantly enhance transverse relaxation rates and generate strong MR signals. *In vivo* results indicate that signals obtained from US imaging from tumors 1 h after injection are enhanced approximately 7-fold. In the case of MR imaging, significantly darkened tumor signals with approximately 16% enhancement were detected after the introduction of SGC. This hybrid nanogel has the potential to be used as a new dual-modality contrast agent for responsive US and T_2-weighted MR imaging.

EXPERIMENTAL SECTION

Synthesis of Functionalized Glycol Chitosan (GCS/acryl/biotin). A 500 mg amount of polysaccharide polymer glycol chitosan was initially dispersed in 100 mL of 2-morpholinoethanesulfonic acid buffer (MES buffer, 0.01 M, pH = 6.5). and stirred overnight at 35 °C. At this time, 33.8 mg of NHS-acrylic acid (about 10% mol of amino group in glycol chitosan) was added to the solution, and the mixture was stirred an additional 5 h. After dialysis at room temperature, 48.8 mg of biotin (about 10% mol of amino group in glycol chitosan) was added to initiate an amidation reaction, using 350 mg of EDC and 450 mg of NHS as activators. The GCS/acryl/biotin solution was then obtained after being dialyzed three times at room temperature against deionized water over 24 h while stirring in order to remove the nonreactive complex.

Synthesis of the Dual-Enzyme-Loaded SPIO Clusters. The monodispersed 6 nm SPIO nanoparticles were prepared using a method reported by Sun *et al.*[60] The SPIO particles in THF (10 mg, 2 mg/mL) were injected into the GCS/acryl/biotin solution (40 mg, 2 mg/mL) and then sonicated for 30 min. SPIO clusters (SPIO@GCS/acryl/biotin) were obtained after dialyzing three times against DI water (5 L), replacing the media for dialysis every 8 h. Catalase (20 mg, 10 mg/mL) and superoxide dismutase (4 mg, 2 mg/mL) in PBS (50 mM phosphate buffer solution, pH = 6.8) were then added into the SPIO@GCS/acryl/biotin solution (20 mg, 2 mg/mL) and stirred at room temperature for another 30 min (GCS/acryl/biotin-CAT/SOD). The dual-enzyme-loaded SPIO clusters (SPIO@GCS/acryl/biotin-CAT/SOD) were centrifuged at 10 000 rpm for 10 min. The supernatant was analyzed in order to calculate the amount of residual enzyme.

Synthesis of Multifunctional Hybrid Nanogel *via* Enzymatic Polymerization. In a typical hydrogelation, 20 mg of bienzyme-loaded clusters (SPIO@GCS/acryl/biotin-CAT/SOD) was dispersed in 100 mL of PBS (pH = 8.5). NHS (10 mL, 10 mM) in PBS (pH = 8.5) and 1 mg of *N*,*N*′-bis(acryloyl)cystamine (4×10^{-3} mmol in 50 μL of methanol) were then added to the above solution while stirring at 25 °C. Finally, 10 mL of laccase (10 U/mL in PBS (pH = 8.5)) was injected into the solution, and the mixture was stirred for an additional hour. The nanogel particles (SGC) were collected by centrifugation.

Loading Amount and Activity Test of CAT and SOD. The loading amount of CAT was determined by the UV absorbance of the residual free CAT in the supernatant liquids. Specifically, the residual CAT in the supernatant liquids can be quantified by the UV absorbance at 403 nm. CAT activity was evaluated based on its ability to degrade H_2O_2 in the examined samples.[61,62] The activity of SGC was determined by adding 100 μL of SGC (50 mM potassium phosphate buffer, pH = 7.0) to 2.9 mL of H_2O_2 solution (0.067 M) and measuring the decrease in absorbance at 206 nm at 25 °C. The activity of the free CAT was also tested as a control by adding 100 μL of CAT solution at the same enzyme concentration found in the SGC nanogels. The specific activity is expressed as the activity of SGC relative to the activity of free CAT: $CAT_{activity}$ (%) = $D \times 100/D_{Free}$, where D and D_{Free} are the H_2O_2 degradation rates (the slope of the absorbance curve) of the CAT-loaded SGC and the free CAT, respectively.

Both the amount and activity of the loaded SOD were assayed based on SOD's ability to inhibit the autoxidation of pyrogallol.[63,64] The autoxidation rate of pyrogallol was determined from the slope of the absorbance curve during the first minute of the reaction. The rate of inhibition is expressed according to the following equation: inhibition (%) = $(A - B) \times 100/A$, where A and B are the autoxidation rates of pyrogallol in the absence and presence of SOD, respectively. The inhibition rate increases linearly with the concentration of pyrogallol when the SOD concentration is lower than 2 μg/mL. The residual SOD in the supernatant liquids was assumed to be free enzyme and can therefore be quantified from the standard curve of the inhibition rate of free SOD. Specifically, 10 μL of pyrogallol (50 mM in 10 mM HCl) and 10 μL of free SOD at various concentrations in 50 mM PBS at pH 7.8 (from 0.05 to 0.125 mg/mL) were added to a quartz cuvette, followed by the injection of Tris-HCl solution (3 mL, 50 mM, pH = 8.2). Dynamic measurements using UV spectroscopy were conducted immediately after injection. The intensity of the absorbance peak at 325 nm was recorded in order to calculate the autoxidation rate. The activity of the SOD is expressed as the specific inhibition rate of the sample relative to the inhibition rate of free SOD: $SOD_{activity}$ (%) = $I \times 100/I_{Free}$, where I and I_{Free} are the rates of inhibition of pyrogallol autoxidation in SOD-loaded SGC and free SOD, respectively.

Enzyme-Sensitive Bubble Generation for Ultrasound Imaging. A clean sheet of glass was dipped into 0.5 mL of SGC solution (5 mg/mL in 50 μM H_2O_2 solution) and covered by a glass slide, excluding all air. An adhesive layer was necessary to fix the SGC solution in place and facilitate observation. The generation of enzyme-sensitive O_2 bubbles from the SGC/H_2O_2 solution (5 mg/mL SGC in 50 μM H_2O_2 solution) as well as the control solution (50 μM H_2O_2) was observed by optical microscopy after approximately 10 s and after 12 h.

Cytotoxicity and Cell Internalization of SGC. Human-derived hepatoma cells (HepG2) were obtained from the Institute of Biochemistry and Cell Biology, Shanghai Institutes of Biological Sciences, Chinese Academy of Sciences (Shanghai, China). Before evaluating SGC's cytotoxicity, the HepG2 cells were cultured in Dulbecco's modified Eagle's medium (DMEM) containing 10% (v/v) fetal bovine serum, 100 units/mL penicillin, and 100 mg/mL streptomycin for 24 h in a 96-well culture plate in a humidified incubator at 37 °C and 5% CO_2. After removing any residual culture medium, 100 μL of SGC solution of different concentrations (100, 200, 400, 500, and 1000 μg/mL in culture medium) was added into each well and co-incubated for another 12 and 24 h. Cell viability was evaluated by adding 3-[4,5-dimethylthiazol-2-yl]-2,5-diphenyltetrazolium bromide (MTT) and using a microplate reader (Bio-Tek ELx800) at a wavelength of 490 nm.

The cell internalization of SGC was further investigated by co-incubating the seeded HepG2 cells with 25, 50, and 100 μg/mL SGC solution for 4 and 8 h in a cell culture dish (NEST Biotech Co., Ltd.). The SGC was first conjugated with the organic fluorescent

FITC using the amino group in SGC to obtain FITC-SGC and facilitate observation by CLSM (Fluo-ViewTM FV1000). After removing the suspending medium and rinsing the cells twice to get rid of any unreacted FITC-SGC, 4′,6-diamidino-2-phenylindole (DAPI, Beyotime Institute of Biotechnology) nuclear stain was added dropwise to the cells for nuclear visualization. Fluorescence images of the cell internalization of SGC were observed by CLSM.

Evaluation of SGC at Relatively High Concentration on Cell Death and Apoptosis. The effect of SGC at relatively high concentration (5 mg/mL) on HepG2 was studied by staining the cells with a combination of the fluorescent DNA-binding dyes AO and EB. Cells were harvested and washed three times with PBS, after being incubated with SGC at 5 mg/mL for 4 and 8 h, and were then stained with AO and EB (AO/EB) for 2 min and observed under a fluorescence microscope. To quantitate apoptosis, prepared cells were washed twice with cold PBS and then resuspended in buffer solution at a concentration of 1×10^6 cells/mL. Annexin V-FITC and PI were then added to these cells and analyzed by flow cytometry.

***T_2* Relaxivity Measurement of SGC *in Vitro*.** Before measuring the T_2 relaxivity, the quantity of Fe element in SGC was determined using ICP-AES (IRIS 1000, Thermo Elemental). Different concentrations of SGC solution *versus* Fe concentration in PBS (100 mM, pH = 7.4) were prepared in the tubes and aligned in the test box. The relaxivity was measured by a 3.0 T clinical MRI instrument (GE Signa HDx 3.0 T). MR T_2 mapping experiments were performed to obtain the T_2 relaxation time with the following parameters: TR = 4000 ms, TE = 13, 26, 39, and 52 ms. Relaxivity values (r_2) were calculated through curve fitting the plot of $1/T_2$ relaxation time (s^{-1}) *versus* Fe concentration (mM). MR images were captured, and the associated data were recorded.

US and MR Imaging of SGC *in Vivo*. All experiments involving animals were ethically and scientifically approved by the University and complied with Practice for Laboratory Animals in China. The New Zealand white rabbits (2.5−3.0 kg) with a VX2 tumor on their livers were supplied by the Laboratory Animals Center of Tenth People's Hospital of Tongji University. The tumor model was built by surgically burying pieces of the VX2 tumor in the rabbit liver and allowing the tumors to grow for an additional 3 weeks.

The rabbits bearing VX2 tumors were shaved prior to US imaging (Mylab ultrasound, ESAOTE, contrast harmonic imaging (CHI) mode, MI = 0.5, Frq = 15 Hz). After the rabbits were anesthetized and fixed, *in vivo* US imaging was conducted before and after intratumoral and intravenous injection of SGC. In order to evaluate the enzyme sensitivity in the tumors, US imaging of the tumors was first conducted after intratumoral injection of SGC and the single enzyme SOD-loaded nanogel (SGC-SOD) (1 mL at 1 and 5 mg/mL) at different times (0, 10, 20, and 30 min). US images and video using both transverse scanning and longitudinal scanning were recorded. In order to further investigate enzyme-responsive US imaging for the tumors, SGC solution (2 mL, 5 mg/mL in PBS) was injected *via* ear vein, and the corresponding US images were captured at different time intervals (0 min, 10 min, 30 min, 1 h, and 2 h) after intravenous injection. The corresponding average gray scales were calculated by using GrayVal 1.0 software (Chongqing Haifu Technology, Chongqing, China). In detail, first the corresponding US images were imported into the software, and a manual-defined ROI was specified as large as the whole tumor area. The gray-scale levels of all pixels within the ROI were averaged by the software, and an average gray-scale value can be therefore obtained. A standard deviation is derived from a group within the ROI (n = 3).

For MRI experiments, the rabbits were first anesthetized and fixed in the MR imaging system (GE Signa HDx 3.0 T). SGC solution (2 mL at 5 mg/mL, about 4 mg/kg) was then administrated *via* an ear vein. MRI was performed with a fast spin−echo sequence (TR/TE = 3740/102 ms (T2), field of view = 21 cm, slice thickness = 5 mm, matrix = 384 × 192). MR imaging of the tumor tissues was conducted prior to injection as well as 15 min, 30 min, 1 h, and 2 h after injection. A single radiologist carried out all quantitative MRI analyses. Signal intensities (SIs) of the tumor tissues were measured in defined ROIs. The change in the relative signal intensities was calculated using SI measurements before (SI_{pre}) and after (SI_{post}) injection of the contrast agents with the formula $[(SI_{post} - SI_{pre})/SI_{pre}] \times 100$. SI_{post} values were collected at different time points. Accumulation of contrast agents within the tumor was further confirmed by *ex vivo* Prussian blue staining images of the tumor tissues 2 h after intravenous injection of SGC. Tumor tissue and other organ tissue (liver, spleen, lung, heart, and kidney) were collected at different time intervals (30 min, 1 h, and 2 h) postinjection investigated by ICP-OES. In addition, the indicated organs from the control animal not injected with SGC were also collected for further analysis in order to avoid any interference by the original Fe element present *in vivo*.

Conflict of Interest: The authors declare no competing financial interest.

Acknowledgment. This work was financially supported by the National Natural Science Foundation of China (51402215, 21274111, 81371570, 51473123), the Program for New Century Excellent Talents in University of Ministry of Education of China (NECT-11-0386), China Postdoctoral Science Foundation (2014M550245), Shanghai Postdoctoral Science Foundation (14R21411200), and the Recruitment Program of Global Experts.

Supporting Information Available: Materials and characterizations; TEM image and magnetization properties of SPIO nanoparticles; TEM image, digital photo, NMR spectra, FT-IR spectra, enzyme loading/activity of SGC; cytotoxicity and cytophagy of SGC; US imaging of SGC using different parameters; pathological examinations of related tumor tissues; ICP-OES analysis of targeted tissues. The Supporting Information is available free of charge on the ACS Publications website at DOI: 10.1021/nn5068094.

REFERENCES AND NOTES

1. Louie, A. Y. Multimodality Imaging Probes: Design and Challenges. *Chem. Rev.* **2010**, *110*, 3146–3195.
2. Massoud, T. F.; Gambhir, S. S. Molecular Imaging in Living Subjects: Seeing Fundamental Biological Processes in a New Light. *Gene Dev.* **2003**, *17*, 545–580.
3. Major, J. L.; Meade, T. J. Bioresponsive, Cell-Penetrating, and Multimeric MR Contrast Agents. *Acc. Chem. Res.* **2009**, *42*, 893–903.
4. Terreno, E.; Delli Castelli, D.; Viale, A.; Aime, S. Challenges for Molecular Magnetic Resonance Imaging. *Chem. Rev.* **2010**, *110*, 3019–3042.
5. Yang, F.; Li, L.; Li, Y.; Chen, Z.; Wu, J.; Gu, N. Superparamagnetic Nanoparticle-Inclusion Microbubbles for Ultrasound Contrast Agents. *Phys. Med. Biol.* **2008**, *53*, 6129–6141.
6. Yang, F.; Li, Y.; Chen, Z.; Zhang, Y.; Wu, J.; Gu, N. Superparamagnetic Iron Oxide Nanoparticle-Embedded Encapsulated Microbubbles as Dual Contrast Agents of Magnetic Resonance and Ultrasound Imaging. *Biomaterials* **2009**, *30*, 3882–3890.
7. Sun, Y.; Zheng, Y.; Ran, H.; Zhou, Y.; Shen, H.; Chen, Y.; Chen, H.; Krupka, T. M.; Li, A.; Li, P.; *et al*. Superparamagnetic PLGA-Iron Oxide Microcapsules for Dual-Modality US/MR Imaging and High Intensity Focused US Breast Cancer Ablation. *Biomaterials* **2012**, *33*, 5854–5864.
8. Ao, M.; Wang, Z.; Ran, H.; Guo, D.; Yu, J.; Li, A.; Chen, W.; Wu, W.; Zheng, Y. Gd-DTPA-Loaded PLGA Microbubbles as Both Ultrasound Contrast Agent and MRI Contrast Agent-a Feasibility Research. *J. Bio. Med. Mater. Res. B* **2010**, *93B*, 551–556.
9. Chen, Y.; Chen, H.; Sun, Y.; Zheng, Y.; Zeng, D.; Li, F.; Zhang, S.; Wang, X.; Zhang, K.; Ma, M.; *et al*. Multifunctional Mesoporous Composite Nanocapsules for Highly Efficient MRI-Guided High-Intensity Focused Ultrasound Cancer Surgery. *Angew. Chem., Int. Ed.* **2011**, *50*, 12505–12509.
10. Niu, D. C.; Wang, X.; Li, Y. S.; Zheng, Y. Y.; Li, F. Q.; Chen, H. R.; Gu, J. L.; Zhao, W. R.; Shi, J. L. Facile Synthesis of Magnetite/Perfluorocarbon Co-Loaded Organic/Inorganic Hybrid Vesicles for Dual-Modality Ultrasound/Magnetic Resonance Imaging and Imaging-Guided High-Intensity

Focused Ultrasound Ablation. *Adv. Mater.* **2013**, *25*, 2686–2692.
11. Albini, A.; Sporn, M. B. The Tumour Microenvironment as a Target for Chemoprevention. *Nat. Rev. Cancer* **2007**, *7*, 139–147.
12. Danhier, F.; Feron, O.; Preat, V. To Exploit the Tumor Microenvironment: Passive and Active Tumor Targeting of Nanocarriers for Anti-Cancer Drug Delivery. *J. Controlled Release* **2010**, *148*, 135–146.
13. Cao, C. Y.; Shen, Y. Y.; Wang, J. D.; Li, L.; Liang, G. L. Controlled Intracellular Self-Assembly of Gadolinium Nanoparticles as Smart Molecular MR Contrast Agents. *Sci. Rep.-Uk* **2013**, *3*, 1024.
14. An, L. N.; Gilani, M. R. H. S.; Liang, G. L. Peptide-Based Nanostructures for Cancer Diagnosis and Therapy. *Curr. Med. Chem.* **2014**, *21*, 2453–2466.
15. Shuhendler, A. J.; Pu, K. Y.; Cui, L.; Uetrecht, J. P.; Rao, J. H. Real-Time Imaging of Oxidative and Nitrosative Stress in the Liver of Live Animals for Drug-Toxicity Testing. *Nat. Biotechnol.* **2014**, *32*, 373–U240.
16. Ye, D. J.; Shuhendler, A. J.; Cui, L. N.; Tong, L.; Tee, S. S.; Tikhomirov, G.; Felsher, D. W.; Rao, J. H. Bioorthogonal Cyclization-Mediated *in Situ* Self-Assembly of Small-Molecule Probes for Imaging Caspase Activity. *in Vivo. Nat. Chem.* **2014**, *6*, 519–526.
17. Fang, J.; Seki, T.; Maeda, H. Therapeutic Strategies by Modulating Oxygen Stress in Cancer and Inflammation. *Adv. Drug Delivery Rev.* **2009**, *61*, 290–302.
18. Barnes, P. J. Immunology of Asthma and Chronic Obstructive Pulmonary Disease. *Nat. Rev. Immunol.* **2008**, *8*, 183–192.
19. Chen, X.; Tian, X.; Shin, I.; Yoon, J. Fluorescent and Luminescent Probes for Detection of Reactive Oxygen and Nitrogen Species. *Chem. Soc. Rev.* **2011**, *40*, 4783–804.
20. Asanuma, D.; Takaoka, Y.; Namiki, S.; Takikawa, K.; Kamiya, M.; Nagano, T.; Urano, Y.; Hirose, K. Acidic-pH-Activatable Fluorescence Probes for Visualizing Exocytosis Dynamics. *Angew. Chem., Int. Ed.* **2014**, *53*, 6085–6089.
21. Ling, D.; Park, W.; Park, S. J.; Lu, Y.; Kim, K. S.; Hackett, M. J.; Kim, B. H.; Yim, H.; Jeon, Y. S.; Na, K.; *et al*. Multifunctional Tumor pH-Sensitive Self-Assembled Nanoparticles for Bimodal Imaging and Treatment of Resistant Heterogeneous Tumors. *J. Am. Chem. Soc.* **2014**, *136*, 5647–5655.
22. Yang, F.; Hu, S. L.; Zhang, Y.; Cai, X. W.; Huang, Y.; Wang, F.; Wen, S.; Teng, G. J.; Gu, N. A Hydrogen Peroxide-Responsive O_2 Nanogenerator for Ultrasound and Magnetic-Resonance Dual Modality Imaging. *Adv. Mater.* **2012**, *24*, 5205–5211.
23. Nayak, S.; Lyon, L. A. Soft Nanotechnology with Soft Nanoparticles. *Angew. Chem., Int. Ed.* **2005**, *44*, 7686–7708.
24. Sasaki, Y.; Akiyoshi, K. Nanogel Engineering for New Nanobiomaterials: From Chaperoning Engineering to Biomedical Applications. *Chem. Rec.* **2010**, *10*, 366–376.
25. Appel, E. A.; Loh, X. J.; Jones, S. T.; Biedermann, F.; Dreiss, C. A.; Scherman, O. A. Ultrahigh-Water-Content Supramolecular Hydrogels Exhibiting Multistimuli Responsiveness. *J. Am. Chem. Soc.* **2012**, *134*, 11767–11773.
26. Li, J. Y.; Li, X. M.; Kuang, Y.; Gao, Y.; Du, X. W.; Shi, J. F.; Xu, B. Self-Delivery Multifunctional Anti-HIV Hydrogels for Sustained Release. *Adv. Healthcare Mater.* **2013**, *2*, 1586–1590.
27. Morris, K. L.; Chen, L.; Raeburn, J.; Sellick, O. R.; Cotanda, P.; Paul, A.; Griffiths, P. C.; King, S. M.; O'Reilly, R. K.; Serpell, L. C.; *et al*. Chemically Programmed Self-Sorting of Gelator Networks. *Nat. Commun.* **2013**, *4*, 1480.
28. Thornton, P. D.; Mart, R. J.; Ulijn, R. V. Enzyme-Responsive Polymer Hydrogel Particles for Controlled Release. *Adv. Mater.* **2007**, *19*, 1252–1256.
29. Thornton, P. D.; Mart, R. J.; Webb, S. J.; Ulijn, R. V. Enzyme-Responsive Hydrogel Particles for the Controlled Release of Proteins: Designing Peptide Actuators to Match Payload. *Soft Matter* **2008**, *4*, 821–827.
30. Kabanov, A. V.; Vinogradov, S. V. Nanogels as Pharmaceutical Carriers: Finite Networks of Infinite Capabilities. *Angew. Chem., Int. Ed.* **2009**, *48*, 5418–5429.
31. Nochi, T.; Yuki, Y.; Takahashi, H.; Sawada, S.; Mejima, M.; Kohda, T.; Harada, N.; Kong, I. G.; Sato, A.; Kataoka, N.; *et al*. Nanogel Antigenic Protein-Delivery System for Adjuvant-Free Intranasal Vaccines. *Nat. Mater.* **2010**, *9*, 572–578.
32. Wang, Q. G.; Yang, Z. M.; Zhang, X. Q.; Xiao, X. D.; Chang, C. K.; Xu, B. A Supramolecular-Hydrogel-Encapsulated Hemin as an Artificial Enzyme to Mimic Peroxidase. *Angew. Chem., Int. Ed.* **2007**, *46*, 4285–4289.
33. Gao, Y.; Zhao, F.; Wang, Q. G.; Zhang, Y.; Xu, B. Small Peptide Nanofibers as the Matrices of Molecular Hydrogels for Mimicking Enzymes and Enhancing the Activity of Enzymes. *Chem. Soc. Rev.* **2010**, *39*, 3425–3433.
34. Kudina, O.; Zakharchenko, A.; Trotsenko, O.; Tokarev, A.; Ionov, L.; Stoychev, G.; Puretskiy, N.; Pryor, S. W.; Voronov, A.; Minko, S. Highly Efficient Phase Boundary Biocatalysis with Enzymogel Nanoparticles. *Angew. Chem., Int. Ed.* **2014**, *53*, 483–487.
35. Paquet, C.; de Haan, H. W.; Leek, D. M.; Lin, H. Y.; Xiang, B.; Tian, G. H.; Kell, A.; Simard, B. Clusters of Superparamagnetic Iron Oxide Nanoparticles Encapsulated in a Hydrogel: A Particle Architecture Generating a Synergistic Enhancement of the T-2 Relaxation. *ACS Nano* **2011**, *5*, 3104–3112.
36. Santra, S.; Jativa, S. D.; Kaittanis, C.; Normand, G.; Grimm, J.; Perez, J. M. Gadolinium-Encapsulating Iron Oxide Nanoprobe as Activatable NMR/MRI Contrast Agent. *ACS Nano* **2012**, *6*, 7281–7294.
37. Courant, T.; Roullin, V. G.; Cadiou, C.; Callewaert, M.; Andry, M. C.; Portefaix, C.; Hoeffel, C.; de Goltstein, M. C.; Port, M.; Laurent, S.; *et al*. Hydrogels Incorporating GdDOTA: Towards Highly Efficient Dual T1/T2MRI Contrast Agents. *Angew. Chem., Int. Ed.* **2012**, *51*, 9119–9122.
38. Hasserodt, J.; Kolanowski, J. L.; Touti, F. Magnetogenesis in Water Induced by a Chemical Analyte. *Angew. Chem., Int. Ed.* **2014**, *53*, 60–73.
39. Hollmann, F.; Arends, I. W. C. E. Enzyme Initiated Radical Polymerizations. *Polymers-Basel* **2012**, *4* (1), 759–793.
40. Su, T.; Zhang, D.; Tang, Z.; Wu, Q.; Wang, Q. G. HRP-Mediated Polymerization Forms Tough Nanocomposite Hydrogels with High Biocatalytic Performance. *Chem. Commun.* **2013**, *49*, 8033–8035.
41. Su, T.; Tang, Z.; He, H. J.; Li, W. J.; Wang, X.; Liao, C. N.; Sun, Y.; Wang, Q. G. Glucose Oxidase Triggers Gelation of N-Hydroxyimide-Heparin Conjugates to Form Enzyme-Responsive Hydrogels for Cell-Specific Drug Delivery. *Chem. Sci.* **2014**, *5*, 4204–4209.
42. Mao, Y. J.; Su, T.; Wu, Q.; Liao, C. A.; Wang, Q. G. Dual Enzymatic Formation of Hybrid Hydrogels with Supramolecular-Polymeric Networks. *Chem. Commun.* **2014**, *50*, 14429–14432.
43. Mates, J. M. Effects of Antioxidant Enzymes in the Molecular Control of Reactive Oxygen Species Toxicology. *Toxicology* **2000**, *153*, 83–104.
44. Fan, J.; Yin, J. J.; Ning, B.; Wu, X. C.; Hu, Y.; Ferrari, M.; Anderson, G. J.; Wei, J. Y.; Zhao, Y. L.; Nie, G. J. Direct Evidence for Catalase and Peroxidase Activities of Ferritin-Platinum Nanoparticles. *Biomaterials* **2011**, *32*, 1611–1618.
45. Okada, S.; Mizukami, S.; Matsumura, Y.; Yoshioka, Y.; Kikuchi, K. A Nanospherical Polymer as an MRI Sensor without Paramagnetic or Superparamagnetic Species. *Dalton Trans.* **2013**, *42*, 15864–15867.
46. Okada, S.; Mizukami, S.; Sakata, T.; Matsumura, Y.; Yoshioka, Y.; Kikuchi, K. Ratiometric MRI Sensors Based on Core-Shell Nanoparticles for Quantitative pH Imaging. *Adv. Mater.* **2014**, *26*, 2989–2992.
47. Shapiro, Y. E. Structure and Dynamics of Hydrogels and Organogels: An NMR Spectroscopy Approach. *Prog. Polym. Sci.* **2011**, *36*, 1184–1253.
48. Crayton, S. H.; Tsourkas, A. pH-Titratable Superparamagnetic Iron Oxide for Improved Nanoparticle Accumulation in Acidic Tumor Microenvironments. *ACS Nano* **2011**, *5*, 9592–9601.
49. Bronstein, L. M.; Huang, X. L.; Retrum, J.; Schmucker, A.; Pink, M.; Stein, B. D.; Dragnea, B. Influence of Iron Oleate Complex Structure on Iron Oxide Nanoparticle Formation. *Chem. Mater.* **2007**, *19*, 3624–3632.

50. Song, N. N.; Yang, H. T.; Ren, X.; Li, Z. A.; Luo, Y.; Shen, J.; Dai, W.; Zhang, X. Q.; Cheng, Z. H. Non-Monotonic Size Change of Monodisperse Fe_3O_4 Nanoparticles in the Scale-up Synthesis. *Nanoscale* **2013**, *5*, 2804–2810.
51. Liu, G. H.; Gan, J. Q.; Chen, A. M.; Liu, Q.; Zhao, X. S. Synthesis and Characterization of an Amphiphilic Chitosan Bearing Octyl and Methoxy Polyethylene. *Nat. Sci.* **2010**, *2*, 707–712.
52. Gupta, A. K.; Wells, S. Surface-Modified Superparamagnetic Nanoparticles for Drug Delivery: Preparation, Characterization, and Cytotoxicity Studies. *IEEE Trans. Nanobiosci.* **2004**, *3*, 66–73.
53. David, C.; d'Andrea, C.; Lancelot, E.; Bochterle, J.; Guillot, N.; Fazio, B.; Marago, O. M.; Sutton, A.; Charnaux, N.; Neubrech, F.; *et al*. Raman and IR Spectroscopy of Manganese Superoxide Dismutase, a Pathology Biomarker. *Vib. Spectrosc.* **2012**, *62*, 50–58.
54. Schutt, E. G.; Klein, D. H.; Mattrey, R. M.; Riess, J. G. Injectable Microbubbles as Contrast Agents for Diagnostic Ultrasound Imaging: The Key Role of Perfluorochemicals. *Angew. Chem., Int. Ed.* **2003**, *42*, 3218–3235.
55. Niu, D. C.; Li, Y. S.; Qiao, X. L.; Li, L.; Zhao, W. R.; Chen, H. R.; Zhao, Q. L.; Ma, Z.; Shi, J. L. A Facile Approach to Fabricate Functionalized Superparamagnetic Copolymer-Silica Nanocomposite Spheres. *Chem. Commun.* **2008**, 4463–4465.
56. Chen, Z. T.; Niu, D. C.; Li, Y. S.; Shi, J. L. One-Step Approach to Synthesize Hollow Mesoporous Silica Spheres Cotemplated by an Amphiphilic Block Copolymer and Cationic Surfactant. *RSC Adv.* **2013**, *3* (19), 6767–6770.
57. Li, L.; Jiang, W.; Luo, K.; Song, H. M.; Lan, F.; Wu, Y.; Gu, Z. W. Superparamagnetic Iron Oxide Nanoparticles as MRI Contrast Agents for Non-invasive Stem Cell Labeling and Tracking. *Theranostics* **2013**, *3*, 595–615.
58. Kinsella, J. M.; Ananda, S.; Andrew, J. S.; Grondek, J. F.; Chien, M. P.; Scadeng, M.; Gianneschi, N. C.; Ruoslahti, E.; Sailor, M. J. Enhanced Magnetic Resonance Contrast of Fe_3O_4 Nanoparticles Trapped in a Porous Silicon Nanoparticle Host. *Adv. Mater.* **2011**, *23*, H248–H253.
59. Wang, X.; Chen, H. R.; Chen, Y.; Ma, M.; Zhang, K.; Li, F. Q.; Zheng, Y. Y.; Zeng, D. P.; Wang, Q.; Shi, J. L. Perfluorohexane-Encapsulated Mesoporous Silica Nanocapsules as Enhancement Agents for Highly Efficient High Intensity Focused Ultrasound (HIFU). *Adv. Mater.* **2012**, *24*, 785–791.
60. Sun, S. H.; Zeng, H.; Robinson, D. B.; Raoux, S.; Rice, P. M.; Wang, S. X.; Li, G. X. Monodisperse MFe_2O_4 (M = Fe, Co, Mn) Nanoparticles. *J. Am. Chem. Soc.* **2004**, *126*, 273–279.
61. Aebi, H. Catalase *in Vitro*. *Methods Enzymol.* **1984**, *105*, 121–126.
62. Beers, R. F., Jr.; Sizer, I. W. A Spectrophotometric Method for Measuring the Breakdown of Hydrogen Peroxide by Catalase. *J. Biol. Chem.* **1952**, *195*, 133–140.
63. Kim, S. J.; Han, D.; Moon, K. D.; Rhee, J. S. Measurement of Superoxide Dismutase-Like Activity of Natural Antioxidants. *Biosci. Biotechnol. Biochem.* **1995**, *59*, 822–826.
64. Gao, R. M.; Yuan, Z. B.; Zhao, Z. Q.; Gao, X. R. Mechanism of Pyrogallol Autoxidation and Determination of Superoxide Dismutase Enzyme Activity. *Bioelectrochem. Bioenerg.* **1998**, *45*, 41–45.